

# Role of exchange splitting in electronic phase competition in $\text{Pb}_{1-x}\text{Sn}_x\text{Te}$

S.Kundu and V.Tripathi

*Department of Theoretical Physics, Tata Institute of Fundamental Research,  
Homi Bhabha Road, Navy Nagar, Colaba, Mumbai-400005*

(Dated: October 23, 2018)

We study the effect of exchange splitting of repulsive interactions on electronic phase transitions in the multiorbital topological crystalline insulator  $\text{Pb}_{1-x}\text{Sn}_x\text{Te}$ , when the chemical potential is tuned to the vicinity of low-lying Type-II Van Hove singularities. Nontrivial Berry phases associated with the Bloch states impart momentum-dependence to electron interactions in the relevant band. We use a “multipatch” parquet renormalization group analysis for studying the competition of different electronic phases, and find that if the dominant fixed-point interactions correspond to antiparallel spin configurations, then a chiral  $p$ -wave Fulde-Ferrell-Larkin-Ovchinnikov (FFLO) state is favoured, otherwise, no phase transition takes place.

Topological crystalline insulators (TCIs) have low-energy surface states in certain high symmetry directions, protected by crystalline symmetry [1]. Unlike conventional  $Z_2$  topological insulators [2–5], the nature of these low-energy states is sensitive to the surface orientation. In particular, it has been shown in the recently discovered TCI  $\text{Pb}_{1-x}\text{Sn}_x\text{Te}$  [6–9] that the bandstructure of the (001) surface allows for the presence of Type-II Van Hove singularities [10], with a diverging density of states which opens up the possibility of a variety of competing Fermi-surface instabilities brought about by weak repulsive interparticle interactions [11–16]. In particular, in a system with multiple Fermi pockets, the parquet approximation has proved very useful in the context of unconventional superconductivity [17–19] in cuprates [20], graphene [21] and semimetal thin films [22]. However, in a multiorbital system like  $\text{Pb}_{1-x}\text{Sn}_x\text{Te}$ , phase competition needs to be studied taking into account the effect of exchange splitting of interactions - something which has not been treated in the above analyses, and is only now beginning to get attention [23].

In this letter, we employ a multipatch parquet renormalization group analysis including exchange splitting effects, and show that even relatively small amounts of exchange splitting ( $|g^{\uparrow\uparrow} - g^{\uparrow\downarrow}| \sim 0.001$ ) can have a dramatic effect on the very existence of electronic instabilities in  $\text{Pb}_{1-x}\text{Sn}_x\text{Te}$ . In contrast, small asymmetries between different scattering channels have no effect on the leading instability. Depending on the sign of the exchange splitting, we find that away from perfect nesting, either a chiral  $p$ -wave FFLO [24, 25] state is stabilized (for  $g^{\uparrow\downarrow} > g^{\uparrow\uparrow}$ ) or no instability occurs (for  $g^{\uparrow\uparrow} > g^{\uparrow\downarrow}$ ) at the level of the parquet approximation. For perfect nesting, spin-density wave (SDW) and charge-density wave (CDW) orders compete with  $p$ -wave superconductivity. A characteristic feature of  $\text{Pb}_{1-x}\text{Sn}_x\text{Te}$  is that the surface bands are effectively spinless, which rules out  $s$ -wave pairing, that would otherwise prevail over  $p$ -wave pairing in the presence of nonmagnetic disorder [26–28].

The topological crystalline insulator surface that we consider offers certain natural advantages from an exper-

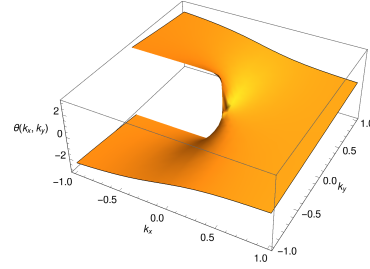


Figure 1. The argument of the effective interaction between electrons with opposite spins  $\sigma$  and  $\bar{\sigma}$ , which shows an  $l=1$  dependence  $\sim \exp[i\theta]$  around the  $\bar{X}$  points

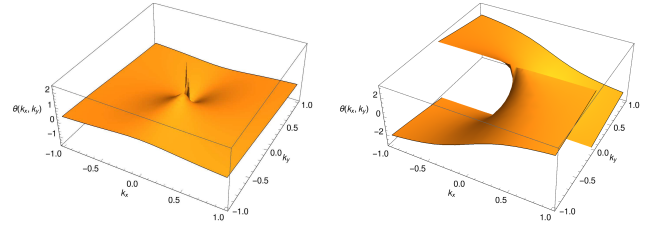


Figure 2. The argument of the effective interaction between electrons with the same spin  $\sigma$  which shows an  $l=0$  dependence or an  $l=2$  dependence  $\sim \exp[2i\theta]$  around the  $\bar{X}$  points

imental point of view. It provides 2D Van Hove singularities which are accessible through a small change in doping, unlike, say, graphene, where a very high level of doping is required. Moreover, as we show below, the  $p$ -wave symmetry originates not from the intrinsic Fermi surface deformations, but from the nontrivial Berry phases associated with the topological states. This is reminiscent of chiral  $p$ -wave superconductivity enabled by a topological Berry phase in fermionic cold atom systems with attractive momentum-independent interactions [29]. We argue that the  $p$ -wave superconductivity on the TCI surface is more robust against potential disorder [30] than in, say,  $\text{Sr}_2\text{RuO}_4$  [31]. Finally, such an FFLO state in a pure solid state system in the absence of an applied magnetic field is a rather unusual occurrence (see, e.g. Refs [32] and [33]). Ref. [34] also discusses an intranode FFLO pairing

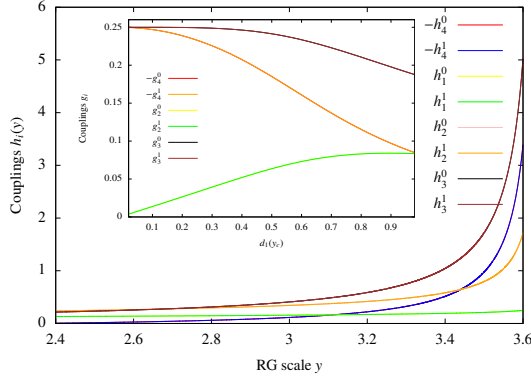


Figure 3. Flow of couplings with renormalization group scale  $y$ , starting with repulsive interactions, where the couplings in different angular momentum channels are assumed to be degenerate initially (here the even angular momentum components are denoted by  $h_i^0$  and the odd angular momentum components by  $h_i^1$ ). We find pair hopping between patches ( $h_3$ ) and on-patch scattering ( $h_4$ ) to be the dominant scattering channels. The inset shows the evolution of the fixed-point couplings  $g_i$  as a function of  $d_1(y_c)$ .

in a doped Weyl semimetal, although the stability of such a state in this system is still a controversial issue [35–37].

The band gap minima of IV-VI semiconductors are located at the four  $L$  points. The TCI surface states are classified into two types: Type-I, for which all four  $L$ -points are projected to the different time-reversal invariant momenta (TRIM) in the surface Brillouin zone, and type-II, for which different  $L$ -points are projected to the same TRIM. The (001) surface falls into the latter class of surfaces, for which  $(L_1, L_2) \rightarrow \overline{X}_1$  and  $(L_3, L_4) \rightarrow \overline{X}_2$ , which leads to two coexisting massless Dirac fermions at  $\overline{X}_1$  arising from the  $L_1$  and the  $L_2$  valley, respectively (and likewise at  $\overline{X}_2$ ). The k.p Hamiltonian close to the point  $\overline{X}_1$  on the (001) surface is derived on the basis of a symmetry analysis in [38], and is given by

$$H_{\overline{X}_1}(k) = (v_x k_x s_y - v_y k_y s_x) + m\tau_x + \delta s_x \tau_y, \quad (1)$$

where  $k$  is measured with respect to  $\overline{X}_1$ ,  $\vec{s}$  is a set of Pauli matrices associated with the two spin components,  $\tau$  operates in valley space, and the terms  $m$  and  $\delta$  are added to describe intervalley scattering. The band dispersion and constant energy contours for the above surface Hamiltonian undergo a Lifshitz transition with increasing energy away from the Dirac point, where two saddle points  $\overline{S}_1$  and  $\overline{S}_2$  at momenta  $(\pm \frac{m}{v_x}, 0)$  lead to a Van-Hove singularity in the density of states. A similar situation arises at the point  $\overline{X}_2$ . We perform our RG analysis with Fermi patches located at these two points  $\overline{X}_1$  and  $\overline{X}_2$  on the (001) surface, near the Van Hove singularities.

In our analysis, we have projected the interactions between electrons in the valley-spin picture to the positive-energy band lying closest to the Van-Hove singularities.

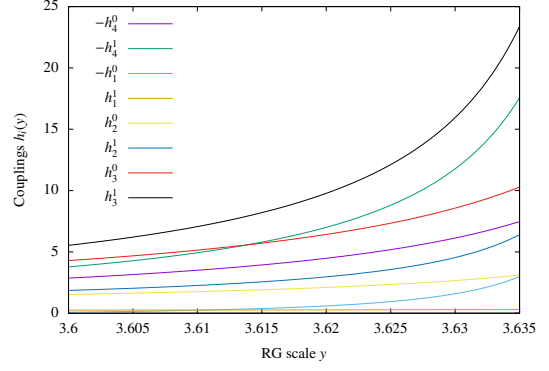


Figure 4. Flow of couplings with renormalization group scale  $y$ , starting with repulsive interactions, where the  $l=1$  components of all the couplings are chosen to larger compared to the  $l=0$  components by 0.1% initially. We find the  $l=1$  components of pair hopping between patches ( $h_3$ ) and on-patch scattering ( $h_4$ ) to be the most dominant couplings in this case.

The resulting coherent factors due to the transformation to the band picture lend a momentum dependence in the form of phase factors to the effective pairing interactions, which arise from the Berry phases of the wavefunctions describing the bands. Figures 1 and 2 show the angular dependence of these different coherent factors, corresponding to antiparallel and parallel spin configurations, respectively. While the former behaves like an  $l=1$  object, the latter show an  $l=0$  or  $l=2$  angular dependence. The low-energy theory within the patch approximation is given by

$$L = \sum_{\alpha, \gamma, \gamma'} \left[ \psi_{\alpha}^{\dagger} (\partial_{\tau} - \epsilon_k + \mu) \psi_{\alpha} - \frac{1}{2} h_4^{\gamma\gamma'} \psi_{\alpha}^{\dagger} \psi_{\alpha}^{\dagger} \psi_{\alpha} \psi_{\alpha} \right. \\ \left. - \sum_{\alpha \neq \beta} \frac{1}{2} (h_1^{\gamma\gamma'} \psi_{\alpha}^{\dagger} \psi_{\beta}^{\dagger} \psi_{\alpha} \psi_{\beta} + h_2^{\gamma\gamma'} \psi_{\alpha}^{\dagger} \psi_{\beta}^{\dagger} \psi_{\beta} \psi_{\alpha} \right. \\ \left. + h_3^{\gamma\gamma'} \psi_{\alpha}^{\dagger} \psi_{\alpha}^{\dagger} \psi_{\beta} \psi_{\beta}) \right], \quad (2)$$

where the summation is over patch labels and the spin structure in each of the terms is given by  $\gamma, \delta, \delta, \gamma$  (where  $\delta = \gamma$  if  $\gamma = \gamma'$  and  $\delta = \overline{\gamma}$  otherwise). Here,  $\epsilon_k$  is obtained by diagonalizing Eq.1. The chemical potential value  $\mu=0$  corresponds to the system being doped to the Van Hove singularities. The different intervalley scattering processes within a patch are represented by a single coupling constant  $h_4$ . The couplings  $h_1, h_2$  and  $h_3$  represent exchange effects, Coulomb interaction and pair hopping, respectively, between electrons on different patches. The even and odd angular momentum channels for each coupling constant are denoted by  $h_i^{\gamma\gamma}$  and  $h_i^{\gamma\overline{\gamma}}$ , respectively. We perform RG analysis up to one-loop level, integrating out high-energy degrees of freedom gradually from an energy cutoff  $\Lambda$ , which is the bandwidth. The susceptibilities in the different channels schematically behave as  $\chi_0^{pp}(\omega) \sim \ln[\Lambda/\omega] \ln[\Lambda/\max(\omega, \mu)]$ ,  $\chi_Q^{ph}(\omega) \sim$

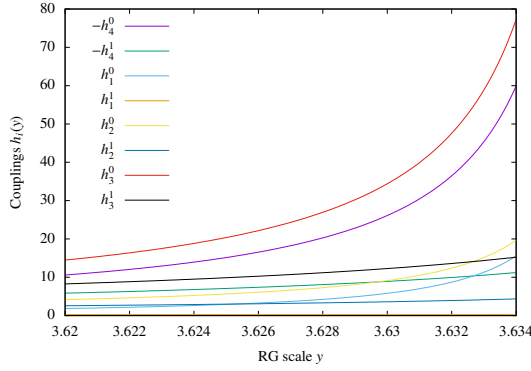


Figure 5. Flow of couplings with renormalization group scale  $y$ , starting with repulsive interactions, where the  $l=0$  components of all the couplings are chosen to be larger compared to the  $l=1$  components by 0.1% initially. We find the  $l=0$  components of pair hopping between patches ( $h_3$ ) and on-patch scattering ( $h_4$ ) to be the most dominant couplings in this case.

$\ln[\Lambda/\max(\omega, \mu)] \ln[\Lambda/\max(\omega, \mu, t)]$  and  $\chi_0^{ph}(\omega), \chi_Q^{pp}(\omega) \sim \ln[\Lambda/\max(\omega, \mu)]$ , where  $\omega$  denotes the energy away from the Van Hove singularities and  $t$  represents terms in the Hamiltonian that destroy the perfect nesting.

We use  $y \equiv \ln^2[\Lambda/\omega] \sim \chi_0^{pp}$  as the RG flow parameter, and describe the relative weight of the other channels as  $d_1(y) = \frac{d\chi_Q^{ph}}{dy}$ ,  $d_2(y) = \frac{d\chi_0^{ph}}{dy}$  and  $d_3(y) = -\frac{d\chi_Q^{pp}}{dy}$ , where  $d_1(y)$  is taken to be a function  $\frac{1}{\sqrt{1+y}}$  [21], interpolating smoothly in between the limits  $d_1(y=0) = 1$  and  $d_1(y \gg 1) = \frac{1}{\sqrt{y}}$ , and  $d_2, d_3 \ll d_1$ . The RG equations are given by

$$\frac{dh_4^{\sigma\sigma}}{dy} = -(2(h_4^{\sigma\sigma})^2 + 2(h_3^{\sigma\sigma})^2), \quad (3)$$

$$\frac{dh_4^{\sigma\bar{\sigma}}}{dy} = -(2(h_4^{\sigma\bar{\sigma}})^2 + 2(h_3^{\sigma\bar{\sigma}})^2), \quad (4)$$

$$\begin{aligned} \frac{dh_1^{\sigma\sigma}}{dy} &= 2d_1(-(h_1^{\sigma\sigma})^2 - (h_3^{\sigma\bar{\sigma}})^2 - (h_1^{\sigma\bar{\sigma}})^2 \\ &\quad + 2h_1^{\sigma\sigma}h_2^{\sigma\sigma} + (h_3^{\sigma\sigma})^2), \end{aligned} \quad (5)$$

$$\frac{dh_1^{\sigma\bar{\sigma}}}{dy} = 2d_1(-2h_1^{\sigma\sigma}h_1^{\sigma\bar{\sigma}} + 2h_1^{\sigma\bar{\sigma}}h_2^{\sigma\sigma}), \quad (6)$$

$$\frac{dh_2^{\sigma\sigma}}{dy} = 2d_1((h_2^{\sigma\sigma})^2 + (h_3^{\sigma\sigma})^2), \quad (7)$$

$$\frac{dh_2^{\sigma\bar{\sigma}}}{dy} = 2d_1((h_2^{\sigma\bar{\sigma}})^2 + (h_3^{\sigma\bar{\sigma}})^2), \quad (8)$$

$$\frac{dh_3^{\sigma\sigma}}{dy} = -4h_4^{\sigma\sigma}h_3^{\sigma\sigma} + 2d_1(4h_2^{\sigma\sigma}h_3^{\sigma\sigma} - 2h_1^{\sigma\bar{\sigma}}h_3^{\sigma\bar{\sigma}}), \quad (9)$$

$$\begin{aligned} \frac{dh_3^{\sigma\bar{\sigma}}}{dy} &= -4h_4^{\sigma\bar{\sigma}}h_3^{\sigma\bar{\sigma}} + 2d_1(2h_2^{\sigma\bar{\sigma}}h_3^{\sigma\bar{\sigma}} \\ &\quad - 2h_1^{\sigma\sigma}h_3^{\sigma\bar{\sigma}} + 2h_2^{\sigma\sigma}h_3^{\sigma\bar{\sigma}}). \end{aligned} \quad (10)$$

These coupled differential equations are then solved, starting from initial values of interactions in the weak-coupling regime ( $h_i^{\gamma\gamma} = h_i^{\gamma\bar{\gamma}} \sim 0.1$ ). The results for the

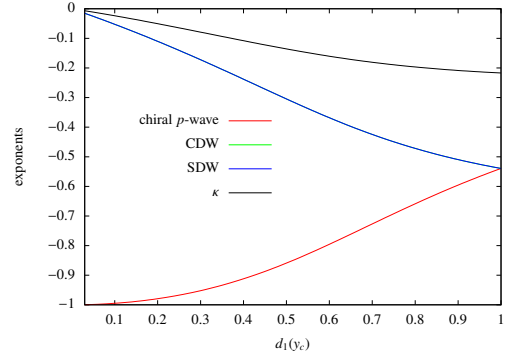


Figure 6. The exponents of various susceptibilities which are negative: chiral  $p$ -wave superconductivity, CDW, SDW and uniform charge compressibility ( $\kappa$ ), for the case where different angular momentum components are chosen to be degenerate initially. These indicate that chiral  $p$ -wave superconductivity is the leading instability throughout, and CDW and SDW are nearly degenerate. However, at  $d_1(y_c) = 1$ , both CDW and SDW instabilities compete with chiral  $p$ -wave superconductivity and all three susceptibilities become equal. This behaviour remains unchanged in the case where  $g^{\uparrow\downarrow} > g^{\uparrow\uparrow}$  initially.

cases where (a) the couplings in different angular momentum channels are degenerate, (b) the couplings in the  $l=1$  channel are assumed to dominate initially, (c) the couplings in the  $l=0$  channel are assumed to dominate initially, are shown in the Fig. 3, 4 and 5 respectively.

We find that renormalization of the cross-patch pair-hopping term  $h_3$  comes from both particle-hole and particle-particle channels. On the other hand, the renormalization of on-patch scattering  $h_4$  comes from the particle-particle channel alone, and those of exchange and Coulomb interactions between patches,  $h_1$  and  $h_2$ , come from the particle-hole channel alone. The low-energy bandstructure has significant nesting in the particle-hole channel, but poor nesting in the particle-particle channel. However, we consider a situation where the nesting between the two patches can be imperfect. Studying the evolution of the RG couplings, we find that while  $h_4$  decreases under RG and eventually goes to  $-\infty$ ,  $h_1$ ,  $h_2$  and  $h_3$  increase and tend to  $\infty$  near the instability threshold.

Each of the couplings have an asymptotic form  $h_i(y) = \frac{g_i^{\sigma\sigma'}}{y_c - y}$  at the threshold. The coefficients  $g_i^{\sigma\sigma'}$  are determined as a function of  $d_1(y_c)$ , and the results for the case, where we start with identical initial values in each of the channels, are shown in the inset in Fig. 3. The exponents  $\alpha$  for various susceptibilities, defined as  $\chi \propto (y_c - y)^\alpha$ , can be calculated using these coefficients. The exponents for intrapatch  $p$ -wave pairing, charge-density wave, spin-density wave, uniform spin, charge compressibility ( $\kappa$ ) and finite-momentum  $\pi$  pairing are given by (see S.I. for

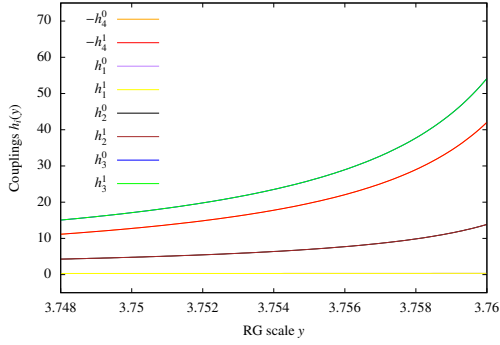


Figure 7. Flow of the couplings with the RG scale  $y$ , with unequal initial values of couplings in different scattering channels while retaining spin degeneracy. Here we have chosen  $h_i^{\sigma\sigma} = h_i^{\sigma\bar{\sigma}}$  but the initial value of  $h_1$  differs from the other  $h_i$  by 10%. The resulting order of coupling values at the fixed-point is identical to the case where all the couplings are chosen to be degenerate initially (see Fig.3).

details)

$$\begin{aligned}
\alpha_{pw} &= 2(-g_3^{\sigma\bar{\sigma}} + g_4^{\sigma\bar{\sigma}}), \\
\alpha_{CDW} &= -2(g_3^{\sigma\bar{\sigma}} - g_1^{\sigma\sigma} - g_1^{\sigma\bar{\sigma}} + g_2^{\sigma\sigma})d_1(y_c), \\
\alpha_{SDW} &= -2(g_3^{\sigma\bar{\sigma}} + g_2^{\sigma\bar{\sigma}})d_1(y_c), \\
\alpha_{\kappa} &= -2(-g_4^{\sigma\bar{\sigma}} - (g_1^{\sigma\sigma} - g_2^{\sigma\sigma} - g_2^{\sigma\bar{\sigma}}))d_2(y_c), \\
\alpha_s &= -2(g_4^{\sigma\bar{\sigma}} + g_1^{\sigma\bar{\sigma}})d_2(y_c), \\
\alpha_{\pi}^{\sigma\sigma} &= 2(g_2^{\sigma\sigma} - g_1^{\sigma\sigma})d_3(y_c), \\
\alpha_{\pi}^{\sigma\bar{\sigma}} &= 2(g_2^{\sigma\bar{\sigma}} - g_1^{\sigma\bar{\sigma}})d_3(y_c).
\end{aligned} \tag{11}$$

The  $p$ -wave order here is chiral since its symmetry is dictated by the  $\exp[i\theta_k]$  dependence of the Berry phase factors in the wavefunctions, and is a finite-momentum pairing. Furthermore, the relative phase of the  $p$ -wave order on different patches is  $\pi$ , which means that we have  $d$ -wave order between the patches (see S.I. for further details).

We do not consider  $s$ - or  $d$ -wave superconductivity since they require spin-singlet Cooper pairing, whereas the electrons here are effectively considered spinless. Figure 6 shows the exponents for  $p$ -wave pairing, SDW, CDW and charge compressibility. Comparison between the values of these exponents shows that the most divergent susceptibility is  $p$ -wave superconductivity throughout the parameter range  $0 < d_1(y_c) < 1$ . The CDW and SDW instabilities show a weaker divergence, and are followed by charge compressibility. The exponents for uniform spin susceptibility and  $\pi$  pairing are always positive and hence, these orders are suppressed. In the case of perfect nesting, i.e  $d_1 = 1$ , the SDW and CDW instabilities become degenerate with  $p$ -wave superconductivity.

Here is a summary of our main findings and their implications. We have studied the role of exchange splitting on phase competition on the (001) surface of the

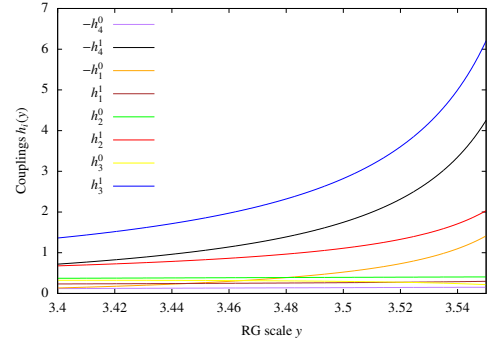


Figure 8. Flow of the couplings with the RG scale  $y$ , with a small lifting (10%) of the spin degeneracy in the scattering channel  $h_1$ , with  $h_1^{\sigma\bar{\sigma}} > h_1^{\sigma\sigma}$ . This changes the order of the couplings at the fixed point drastically, and the couplings  $h_3^{\sigma\bar{\sigma}}$  and  $h_4^{\sigma\bar{\sigma}}$  now dominate the rest of the couplings in the RG flow.

crystalline topological insulator  $\text{Pb}_{1-x}\text{Sn}_x\text{Te}$ , featuring type-II Van Hove singularities. Our central result is that the electronic stabilities in this system are very sensitive to the nature of the exchange splitting, and the leading instability for dominant antiparallel spin configurations is an intrapatch FFLO state, while for dominant parallel spin configurations, no instability is obtained within this approach. It is important to note that we have  $p$ -wave order on the patches, unlike [10] and [22]. In contrast, a similar lifting of the degeneracy of interactions in different scattering channels has no effect on the instabilities. This is demonstrated in the Fig. 7 and 8. We find that spin-splitting along certain scattering channels, specifically, pair hopping between different patches and on-patch scattering, affects the results more drastically than others in the weak-coupling limit, due to the larger contribution to the logarithmic singularities from these channels. The absence of any instability when  $g^{\uparrow\uparrow} > g^{\uparrow\downarrow}$  is directly related to the effectively spinless nature of the electrons in the band, due to which superconductivity in even angular momentum channels is not possible. Interestingly, we find that subtle cancellations between contributions from different scattering channels conspire to rule out the possibility of competing instabilities like CDW or SDW taking over in the case when  $p$ -wave superconductivity is unstable, even in the case of perfect nesting.

We now discuss the effects of weak disorder on superconductivity on our crystalline topological insulator surface. Since potential scattering of the electrons changes their momenta, we expect the  $d$ -wave pairing across the patches to be sensitive to such disorder. However, within a patch, the  $p$ -wave pairing is topologically protected. To see this, note that our order parameter  $\langle \psi_k \psi_{-k} \rangle \sim \Delta_0 \exp[i\theta_k]$  (where  $\psi$  denotes the spinless fermion in the relevant band and  $\theta_k$  arises from the nontrivial Berry phases). Translated to the valley-spin picture, this shows that the superconducting order pa-

parameter in terms of those fermions has no momentum dependence, and hence, cannot be degraded by weak potential disorder.

Finally, we discuss the experimental implications of our work. Recently, there have been reports of surface superconductivity induced on the surface of  $\text{Pb}_{0.6}\text{Sn}_{0.4}\text{Te}$  by forming a mesoscopic point contact using a nonsuperconducting metal [39]. The observed transition temperature is in the range 3.7-6.5 K. We expect transition temperatures roughly an order of magnitude smaller than the bandwidth  $\Lambda$ , which is of the order of the bandgap. How-

ever, the nature of the Cooper pair order in the experiment is not yet settled and further experimental work needs to be done in this direction to confirm our prediction of surface  $p$ -wave superconductivity in this material. Our approach could also be useful for studying phase competition in other two-dimensional systems with multiple Fermi pockets in the presence of exchange splitting.

VT acknowledges DST for a Swarnajayanti grant (No. DST/SJF/PSA-0212012-13).

---

### Supplementary material for Role of exchange splitting in electronic phase competition in $\text{Pb}_{1-x}\text{Sn}_x\text{Te}$ :

Here we provide additional information on 1) electron interactions in the valley-spin picture and effective interactions when projected to a band, 2) coupling renormalization and 3) calculation of susceptibilities corresponding to different channels.

#### Interactions between electrons on different valleys:

For the (001) surface of SnTe, different  $L$ -points are projected to the same surface momenta. In particular,  $(L_1, L_2) \rightarrow \overline{X}_1$  and  $(L_3, L_4) \rightarrow \overline{X}_2$ . As a result, there is interaction between electrons on different  $L$ -valleys. Two coexisting massless Dirac fermions arise at  $\overline{X}_1$  from the  $L_1$  and  $L_2$  valley, respectively, and likewise for  $\overline{X}_2$ . Let us consider different interactions between the valleys  $L_1$  and  $L_2$  corresponding to the  $\overline{X}_1$  point, for various spin combinations-

$$H_I = U_1 \sum_a c_{\alpha a}^\dagger c_{\beta a}^\dagger c_{\beta a} c_{\alpha a} + U_2 \sum_{a \neq b} c_{\alpha a}^\dagger c_{\beta b}^\dagger c_{\beta b} c_{\alpha a} + J_1 \sum_{a \neq b} c_{\alpha a}^\dagger c_{\beta b}^\dagger c_{\beta a} c_{\alpha b} + J_2 \sum_{a \neq b} c_{\alpha a}^\dagger c_{\beta a}^\dagger c_{\beta b} c_{\alpha b}$$

where the  $U_1$  term corresponds to Coulomb interaction between electrons on the same valley,  $U_2$  represents interactions between electrons on different valleys.  $J_1$  represents the exchange effect favoring parallel spins on the same valley and  $J_2$  is the pair hopping between different valleys. For the k.p Hamiltonian  $H_{\overline{X}_1}(k)$  of the (001) surface, the operators corresponding to different bands can be rewritten in terms of the operators for different valley and spin combinations as follows-

$$\begin{aligned} \psi_1 &= a_1 c_{\uparrow 1} + b_1 c_{\downarrow 1} + c_1 c_{\uparrow 2} + d_1 c_{\downarrow 2}, \\ \psi_2 &= a_2 c_{\uparrow 3} + b_2 c_{\downarrow 3} + c_2 c_{\uparrow 4} + d_2 c_{\downarrow 4}, \\ \psi_3 &= a_3 c_{\uparrow 1} + b_3 c_{\downarrow 1} + c_3 c_{\uparrow 2} + d_3 c_{\downarrow 2}, \\ \psi_4 &= a_4 c_{\uparrow 3} + b_4 c_{\downarrow 3} + c_4 c_{\uparrow 4} + d_4 c_{\downarrow 4}, \\ \psi_5 &= a_5 c_{\uparrow 1} + b_5 c_{\downarrow 1} + c_5 c_{\uparrow 2} + d_5 c_{\downarrow 2}, \\ \psi_6 &= a_6 c_{\uparrow 3} + b_6 c_{\downarrow 3} + c_6 c_{\uparrow 4} + d_6 c_{\downarrow 4}, \\ \psi_7 &= a_7 c_{\uparrow 1} + b_7 c_{\downarrow 1} + c_7 c_{\uparrow 2} + d_7 c_{\downarrow 2}, \\ \psi_8 &= a_8 c_{\uparrow 3} + b_8 c_{\downarrow 3} + c_8 c_{\uparrow 4} + d_8 c_{\downarrow 4}, \end{aligned} \tag{12}$$

where the  $\{a_i, b_i, c_i, d_i, i = 1 \text{ to } 8\}$  correspond to the components of the eigenvectors of the Hamiltonian, and are functions of  $k_x$  and  $k_y$  in the 2D surface Brillouin zone. Since the points  $\overline{X}$  are decoupled from each other, 4 of these components for each eigenvector vanish. We can invert the above equations to write the  $c'_{\alpha a}$ s in terms of  $\psi'_i$ s. Now, we are only interested in the two lower bands which lie in the bulk band gap and are closer to the saddle points in energy. In particular, we shall concentrate on the positive energy bands closer to the saddle points for each of the  $\overline{X}$ , in which case we can drop all the terms from the above equations except those involving  $\psi_3$  and  $\psi_4$ , the relevant bands. We then have  $c_{\uparrow 1} = u_{\uparrow 1} \psi_3$ ,  $c_{\downarrow 1} = u_{\downarrow 1} \psi_3$ ,  $c_{\uparrow 2} = u_{\uparrow 2} \psi_3$  and  $c_{\downarrow 2} = u_{\downarrow 2} \psi_3$ , and likewise for  $\psi_4$ , suppressing the contributions from the other bands. Substituting all of these expressions into  $H_I$  above, and writing  $c_{\alpha a}$  generally as

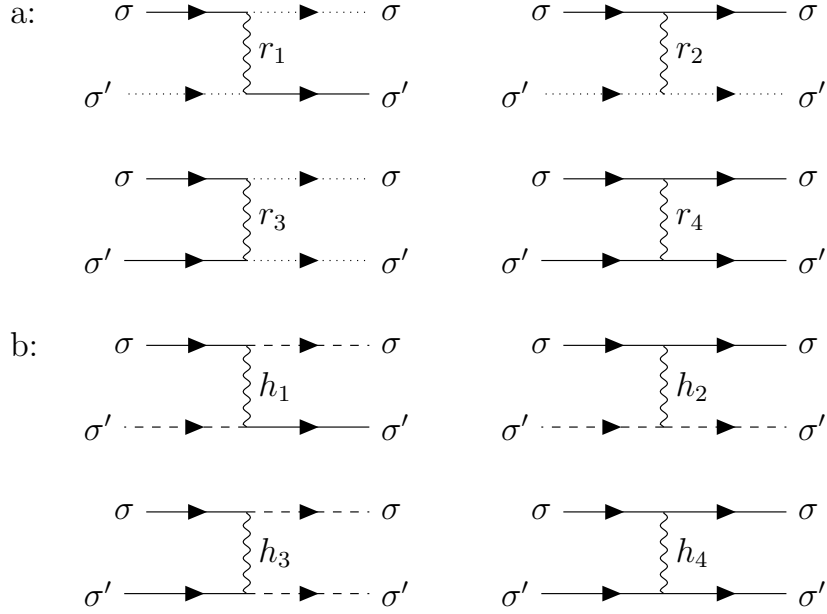


Figure 9. (a) Couplings defined on a patch, (b) Couplings between different patches

$\sum_i u_{\alpha i} \psi_i$ , we have

$$\begin{aligned}
H_I = & U_1 \sum_{k_1, k_2, k'_1, a} \sum_{i, j, k, l} u_{\alpha a i}^*(k'_1) u_{\beta a j}^*(k'_2) u_{\beta a k}(k_1) u_{\alpha a l}(k_2) \psi_i^\dagger(k'_1) \psi_j^\dagger(k'_2) \psi_k(k_1) \psi_l(k_2) \\
& + U_2 \sum_{k_1, k_2, k'_1, a \neq b} \sum_{i, j, k, l} u_{\alpha a i}^*(k'_1) u_{\beta b j}^*(k'_2) u_{\beta b k}(k_1) u_{\alpha a l}(k_2) \psi_i^\dagger(k'_1) \psi_j^\dagger(k'_2) \psi_k(k_1) \psi_l(k_2) \\
& + J_1 \sum_{k_1, k_2, k'_1, a \neq b} \sum_{i, j, k, l} u_{\alpha a i}^*(k'_1) u_{\beta b j}^*(k'_2) u_{\beta a k}(k_1) u_{\alpha b l}(k_2) \psi_i^\dagger(k'_1) \psi_j^\dagger(k'_2) \psi_k(k_1) \psi_l(k_2) \\
& + J_2 \sum_{k_1, k_2, k'_1, a \neq b} \sum_{i, j, k, l} u_{\alpha a i}^*(k'_1) u_{\beta a j}^*(k'_2) u_{\beta b k}(k_1) u_{\alpha b l}(k_2) \psi_i^\dagger(k'_1) \psi_j^\dagger(k'_2) \psi_k(k_1) \psi_l(k_2), \tag{13}
\end{aligned}$$

where  $k_1, k_2, k'_1, k'_2$  are constrained by momentum conservation, and  $i, j, k$  and  $l$  correspond to different bands. In practice, the expression is considerably simplified since only certain bands contribute for a given valley and we further consider only the ones closest to the saddle points. This leads to the four kinds of allowed interactions between the electrons belonging to the different  $\bar{X}$  points.

### Coupling renormalization:

The RG equations are obtained by evaluating second-order diagrams and collecting the respective combinatoric prefactors, for each of the interactions  $h_1, h_2, h_3$  and  $h_4$ . The coupling vertices for interactions (a)  $r_i$  on a patch (each of which is replaced by  $h_4$  in our RG equations) and (b) between the two patches, are shown in Fig. 9. The diagrams corresponding to the renormalization of the interaction  $h_2$  is shown in Fig. 10.

### Susceptibilities:

We now investigate the instabilities of the system by evaluating the susceptibilities  $\chi$  for various types of order, introducing infinitesimal test vertices corresponding to different kinds of pairing into the action, such as  $\Delta_\alpha c_{\alpha\sigma}^\dagger c_{\alpha\sigma'}^\dagger + \Delta_\alpha^* c_{\alpha\sigma} c_{\alpha\sigma'}$  for the patch  $\alpha$  corresponding to particle-particle pairing on the patch. The diagrams corresponding to the renormalization of the different kinds of pairing vertices are given in Fig. 11.

The renormalization of the test vertex corresponding to particle-particle pairing on a patch is governed by the equation

$$\frac{d}{dy} \begin{pmatrix} \Delta_1 \\ \Delta_2 \end{pmatrix} = \begin{pmatrix} 2h_4^{\sigma\bar{\sigma}} & 2h_3^{\sigma\bar{\sigma}} \\ 2h_3^{\sigma\bar{\sigma}} & 2h_4^{\sigma\bar{\sigma}} \end{pmatrix} \begin{pmatrix} \Delta_1 \\ \Delta_2 \end{pmatrix}$$

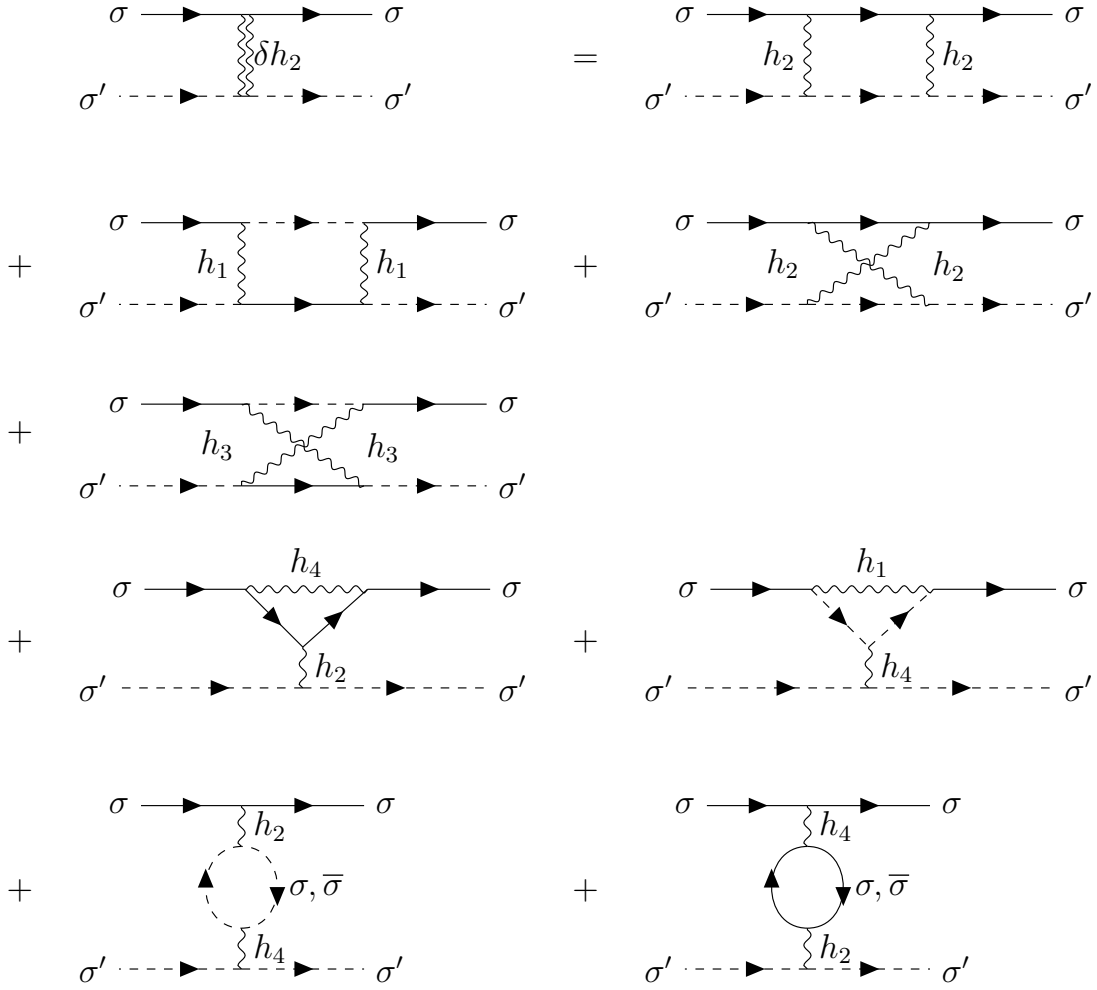


Figure 10. Diagrams for one-loop renormalization of the coupling  $h_2$ . The diagrams for  $h_1$ ,  $h_3$  and  $h_4$  are similarly obtained.

since we can only consider Cooper pairing in the  $p$ -wave channel for spinless electrons. By transforming to the eigenvalue basis, we can obtain different possible order parameters, and choose the one corresponding to the most negative eigenvalue. The vertices with positive eigenvalues are suppressed under RG flow.

Similarly, the renormalization of the test vertex corresponding to particle-hole pairing between the patches, in the  $l=0$  channel is given by

$$\frac{d}{dy} \begin{pmatrix} \Delta_{12} \\ \Delta_{21} \end{pmatrix} = -d_1(y) \begin{pmatrix} 2h_2^{\sigma\sigma} - 2h_1^{\sigma\sigma} - 2h_1^{\sigma\bar{\sigma}} & -2h_3^{\sigma\bar{\sigma}} \\ -2h_3^{\sigma\bar{\sigma}} & 2h_2^{\sigma\sigma} - 2h_1^{\sigma\sigma} - 2h_1^{\sigma\bar{\sigma}} \end{pmatrix} \begin{pmatrix} \Delta_{12} \\ \Delta_{21} \end{pmatrix}$$

and in the  $l=1$  channel, by

$$\frac{d}{dy} \begin{pmatrix} \Delta_{12} \\ \Delta_{21} \end{pmatrix} = -d_1(y) \begin{pmatrix} 2h_2^{\sigma\bar{\sigma}} & 2h_3^{\sigma\bar{\sigma}} \\ 2h_3^{\sigma\bar{\sigma}} & 2h_2^{\sigma\bar{\sigma}} \end{pmatrix} \begin{pmatrix} \Delta_{12} \\ \Delta_{21} \end{pmatrix}$$

The renormalization of the test vertex corresponding to particle-particle pairing between the patches, in the  $l=0$  channel, is given by

$$\frac{d}{dy} \begin{pmatrix} \Delta_{12} \\ \Delta_{21} \end{pmatrix} = d_3(y) \begin{pmatrix} 2h_2^{\sigma\sigma} & 2h_1^{\sigma\sigma} \\ 2h_1^{\sigma\sigma} & 2h_2^{\sigma\sigma} \end{pmatrix} \begin{pmatrix} \Delta_{12} \\ \Delta_{21} \end{pmatrix}$$

and in the  $l=1$  channel, by

$$\frac{d}{dy} \begin{pmatrix} \Delta_{12} \\ \Delta_{21} \end{pmatrix} = d_3(y) \begin{pmatrix} 2h_2^{\sigma\bar{\sigma}} & 2h_1^{\sigma\bar{\sigma}} \\ 2h_1^{\sigma\bar{\sigma}} & 2h_2^{\sigma\bar{\sigma}} \end{pmatrix} \begin{pmatrix} \Delta_{12} \\ \Delta_{21} \end{pmatrix}$$

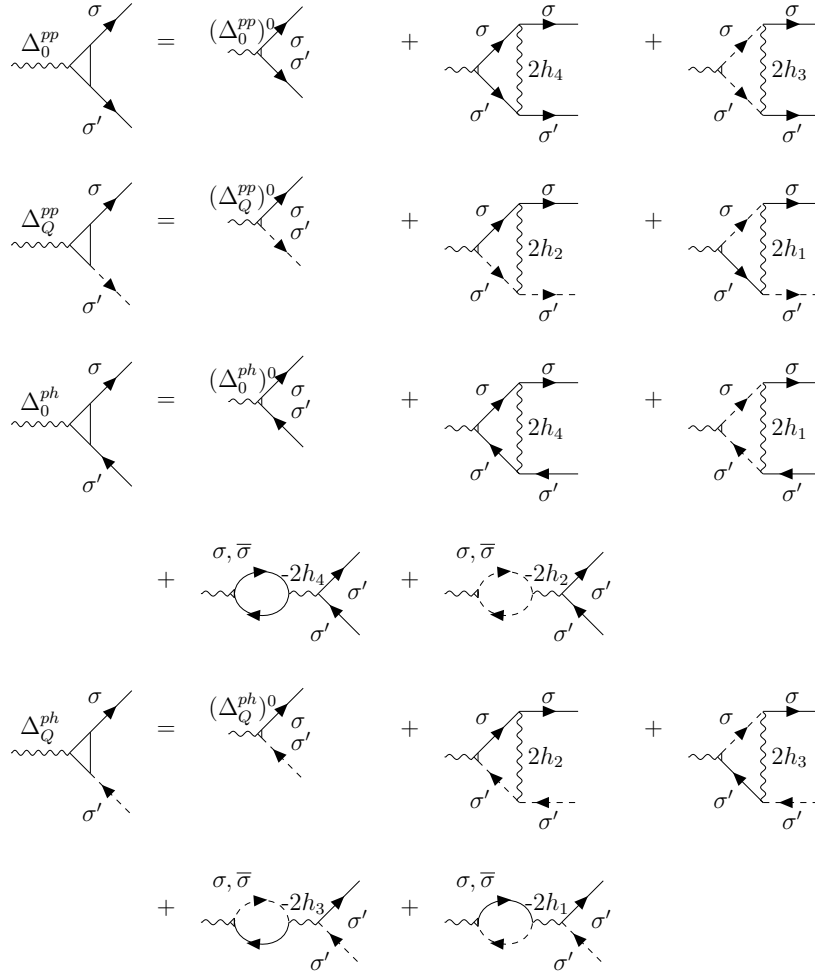


Figure 11. Vertex renormalization corresponding to (a) particle-particle pairing on the patch, (b) particle-particle pairing between patches, (c) particle-hole pairing on the patch and (d) particle-hole pairing between patches.

The renormalization of the test vertex corresponding to particle-hole pairing on a patch, in the  $l=0$  channel, is given by

$$\frac{d}{dy} \begin{pmatrix} \Delta_1 \\ \Delta_2 \end{pmatrix} = -d_2(y) \begin{pmatrix} -2h_4^{\sigma\bar{\sigma}} & 2h_1^{\sigma\sigma} - 2h_2^{\sigma\sigma} - 2h_2^{\sigma\bar{\sigma}} \\ 2h_1^{\sigma\sigma} - 2h_2^{\sigma\sigma} - 2h_2^{\sigma\bar{\sigma}} & -2h_4^{\sigma\bar{\sigma}} \end{pmatrix} \begin{pmatrix} \Delta_1 \\ \Delta_2 \end{pmatrix}$$

and in the  $l=1$  channel, is given by

$$\frac{d}{dy} \begin{pmatrix} \Delta_1 \\ \Delta_2 \end{pmatrix} = -d_2(y) \begin{pmatrix} 2h_4^{\sigma\bar{\sigma}} & 2h_1^{\sigma\bar{\sigma}} \\ 2h_1^{\sigma\bar{\sigma}} & 2h_4^{\sigma\bar{\sigma}} \end{pmatrix} \begin{pmatrix} \Delta_1 \\ \Delta_2 \end{pmatrix}$$

The most negative eigenvalue corresponding to Cooper pairing on the patch is given by  $2(-h_3^{\sigma\bar{\sigma}} + h_4^{\sigma\bar{\sigma}})$  which corresponds to the eigenvector  $\frac{1}{\sqrt{2}} \begin{pmatrix} -1 & 1 \end{pmatrix}$ , competing with those corresponding to CDW and SDW order, given by  $-2(h_3^{\sigma\bar{\sigma}} - h_1^{\sigma\sigma} - h_1^{\sigma\bar{\sigma}} + h_2^{\sigma\sigma})d_1(y)$  (corresponding to the eigenvector  $\frac{1}{\sqrt{2}} \begin{pmatrix} -1 & 1 \end{pmatrix}$ ) and  $-2(h_3^{\sigma\bar{\sigma}} + h_2^{\sigma\bar{\sigma}})d_1(y)$  (corresponding to the eigenvector  $\frac{1}{\sqrt{2}} \begin{pmatrix} 1 & 1 \end{pmatrix}$ ) respectively. This is followed by particle-hole pairing on a patch in the  $l=0$  channel, with the more negative eigenvalue given by  $-2(-h_4^{\sigma\bar{\sigma}} - (h_1^{\sigma\sigma} - h_2^{\sigma\sigma} - h_2^{\sigma\bar{\sigma}}))d_2(y)$  (corresponding to the eigenvector  $\frac{1}{\sqrt{2}} \begin{pmatrix} -1 & 1 \end{pmatrix}$ ). Thus, the dominant instability of our system, namely  $p$ -wave superconductivity, appears in the  $l=1$  channel, whereas the dominant coupling in the  $l=0$  channel does not lead to any instability due to the absence of  $s$ - or  $d$ -wave superconductivity on the patch.

The vertices flow to different strong coupling fixed points with an asymptotic form  $h_i(y) = \frac{g_i^{\sigma\sigma'}}{y_c - y}$ , with  $y_c$  being the critical point of the one-loop RG equations. This asymptotic form is substituted into the Eq.3-10 to obtain the polynomial equations



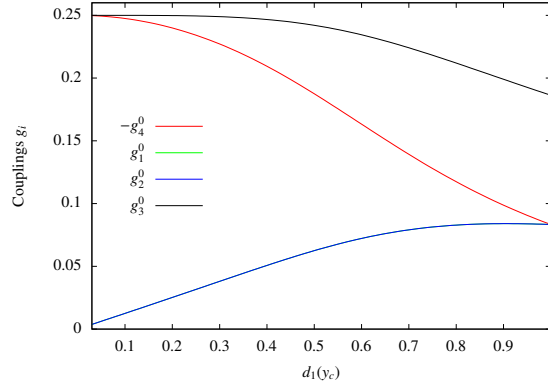


Figure 12. The fixed point values for  $g_i$  as a function of  $d_1(y_c)$  for the case where the  $l=0$  components of all the couplings are assumed to be greater initially

$$\begin{aligned}
g_4^{\sigma\sigma} &= -2(g_4^{\sigma\sigma}) - 2(g_3^{\sigma\sigma})^2, \\
g_4^{\sigma\bar{\sigma}} &= -2(g_4^{\sigma\bar{\sigma}})^2 - 2(g_3^{\sigma\bar{\sigma}})^2, \\
g_1^{\sigma\sigma} &= 2d_1(y_c)(-(g_1^{\sigma\sigma})^2 - (g_3^{\sigma\bar{\sigma}})^2 - (g_1^{\sigma\bar{\sigma}})^2 \\
&\quad + 2g_1^{\sigma\sigma}g_2^{\sigma\sigma} + (g_3^{\sigma\sigma})^2), \\
g_1^{\sigma\bar{\sigma}} &= 2d_1(y_c)(-2g_1^{\sigma\sigma}g_1^{\sigma\bar{\sigma}} + 2g_1^{\sigma\bar{\sigma}}g_2^{\sigma\sigma}), \\
g_2^{\sigma\sigma} &= 2d_1(y_c)((g_2^{\sigma\sigma})^2 + (g_3^{\sigma\sigma})^2), \\
g_2^{\sigma\bar{\sigma}} &= 2d_1(y_c)((g_2^{\sigma\bar{\sigma}})^2 + (g_3^{\sigma\bar{\sigma}})^2), \\
g_3^{\sigma\sigma} &= -4g_4^{\sigma\sigma}g_3^{\sigma\sigma} + 2d_1(y_c)(4g_2^{\sigma\sigma}g_3^{\sigma\sigma} - 2g_1^{\sigma\bar{\sigma}}g_3^{\sigma\bar{\sigma}}), \\
g_3^{\sigma\bar{\sigma}} &= -4g_4^{\sigma\bar{\sigma}}g_3^{\sigma\bar{\sigma}} + 2d_1(y_c)(2g_2^{\sigma\bar{\sigma}}g_3^{\sigma\bar{\sigma}} \\
&\quad - 2g_1^{\sigma\sigma}g_3^{\sigma\bar{\sigma}} + 2g_2^{\sigma\sigma}g_3^{\sigma\bar{\sigma}}).
\end{aligned} \tag{14}$$

In the case where the spin degeneracy is broken, the fixed point values of the couplings  $g_i^{\sigma\sigma'}$  can take different values for a given value of  $d_1(y_c)$ , depending on the initial order of these couplings. However, in the two special cases where all the couplings corresponding to a particular angular momentum channel are taken to be equal and larger than the other channel, one can obtain plots for the couplings  $g_i^{\sigma\sigma'}$  as a function of  $d_1(y_c)$ . This is shown in Fig. 12 for the case where  $l=0$  couplings are dominant.

The various susceptibilities  $\chi$  then diverge as  $(y_c - y)^\alpha$  and the exponents  $\alpha$  for p-wave pairing, CDW, SDW and uniform charge compressibility are given by

$$\begin{aligned}
\alpha_{\text{pw}} &= 2(-g_3^{\sigma\bar{\sigma}} + g_4^{\sigma\bar{\sigma}}), \\
\alpha_{\text{CDW}} &= -2(g_3^{\sigma\bar{\sigma}} - g_1^{\sigma\sigma} - g_1^{\sigma\bar{\sigma}} + g_2^{\sigma\sigma})d_1(y_c), \\
\alpha_{\text{SDW}} &= -2(g_3^{\sigma\bar{\sigma}} + g_2^{\sigma\bar{\sigma}})d_1(y_c), \\
\alpha_\kappa &= -2(-g_4^{\sigma\bar{\sigma}} - (g_1^{\sigma\sigma} - g_2^{\sigma\sigma} - g_2^{\sigma\bar{\sigma}}))d_2(y_c).
\end{aligned}$$

We can compare the values of these to find that the most divergent susceptibility throughout the parameter region of  $0 < d_1(y_c) < 1$ , which turns out to be p-wave pairing on the patch.

- 
- [1] L. Fu, Phys. Rev. Lett. **106**, 106802 (2011).  
[2] M. Z. Hasan and C. L. Kane, Rev. Mod. Phys. **82**, 3045 (2010).

- 
- [3] M. König, H. Buhmann, L. W. Molenkamp, T. Hughes, C.-X. Liu, X.-L. Qi, and S.-C. Zhang, J. Phys. Soc. Jpn. **77**, 031007 (2008).  
[4] J. E. Moore, Nature **464**, 194 (2010).  
[5] X.-L. Qi and S.-C. Zhang, Rev. Mod. Phys. **83**, 1057 (2011).

- [6] P. Dziawa, B. Kowalski, K. Dybko, R. Buczko, A. Szczerbakow, M. Szot, E. Łusakowska, T. Balasubramanian, B. M. Wojek, M. Berntsen, *et al.*, Nat. Mater **11**, 1023 (2012).
- [7] T. H. Hsieh, H. Lin, J. Liu, W. Duan, A. Bansil, and L. Fu, Nat. Commun **3**, 982 (2012).
- [8] Y. Tanaka, Z. Ren, T. Sato, K. Nakayama, S. Souma, T. Takahashi, K. Segawa, and Y. Ando, Nat. Phys. **8**, 800 (2012).
- [9] S.-Y. Xu, C. Liu, N. Alidoust, M. Neupane, D. Qian, I. Belopolski, J. Denlinger, Y. Wang, H. Lin, L. Wray, *et al.*, Nat. Commun **3**, 1192 (2012).
- [10] H. Yao and F. Yang, Phys. Rev. B **92**, 035132 (2015).
- [11] I. Dzyaloshinskii, JETP Lett **46** (1987).
- [12] H. Schulz, EPL **4**, 609 (1987).
- [13] P. Lederer, G. Montambaux, and D. Poilblanc, J. Phys. **48**, 1613 (1987).
- [14] D. Yudin, D. Hirschmeier, H. Hafermann, O. Eriksson, A. I. Lichtenstein, and M. I. Katsnelson, Phys. Rev. Lett. **112**, 070403 (2014).
- [15] R. Nandkishore, R. Thomale, and A. V. Chubukov, Phys. Rev. B **89**, 144501 (2014).
- [16] Z. Y. Meng, F. Yang, K.-S. Chen, H. Yao, and H.-Y. Kee, Phys. Rev. B **91**, 184509 (2015).
- [17] V. P. Mineev, K. Samokhin, and L. Landau, *Introduction to unconventional superconductivity* (CRC Press, 1999).
- [18] M. R. Norman, Science **332**, 196 (2011).
- [19] M. Sigrist and K. Ueda, Rev. Mod. Phys. **63**, 239 (1991).
- [20] N. Furukawa, T. Rice, and M. Salmhofer, Phys. Rev. Lett. **81**, 3195 (1998).
- [21] R. Nandkishore, L. Levitov, and A. Chubukov, Nat. Phys **8**, 158 (2012).
- [22] J.-Q. Huang, C.-H. Hsu, H. Lin, D.-X. Yao, and W.-F. Tsai, Phys. Rev. B **93**, 155108 (2016).
- [23] J. Yuan and C. Honerkamp, arXiv preprint arXiv:1504.04536 (2015).
- [24] P. Fulde and R. A. Ferrell, Phys. Rev. **135**, A550 (1964).
- [25] A. Larkin and Y. N. Ovchinnikov, Zh. Eksperim. i Teor. Fiz. **47** (1964).
- [26] R. Balian and N. R. Werthamer, Phys. Rev. **131**, 1553 (1963).
- [27] A. P. Mackenzie and Y. Maeno, Rev. Mod. Phys. **75**, 657 (2003).
- [28] P. W. Anderson, J. Phys. Chem. Solids **11**, 26 (1959).
- [29] C. Zhang, S. Tewari, R. M. Lutchyn, and S. D. Sarma, Phys. Rev. Lett. **101**, 160401 (2008).
- [30] K. Michaeli and L. Fu, Phys. Rev. Lett. **109**, 187003 (2012).
- [31] A. P. Mackenzie, R. K. W. Haselwimmer, A. W. Tyler, G. G. Lonzarich, Y. Mori, S. Nishizaki, and Y. Maeno, Phys. Rev. Lett. **80**, 161 (1998).
- [32] K. Kubo, J. Phys. Soc. Jpn. **77**, 043702 (2008).
- [33] Y.-T. Hsu, A. Vaezi, M. H. Fischer, and E.-A. Kim, arXiv preprint arXiv:1606.00857 (2016).
- [34] G. Y. Cho, J. H. Bardarson, Y.-M. Lu, and J. E. Moore, Phys. Rev. B **86**, 214514 (2012).
- [35] G. Bednik, A. Zyuzin, and A. Burkov, Phys. Rev. B **92**, 035153 (2015).
- [36] H. Wei, S.-P. Chao, and V. Aji, Phys. Rev. B **89**, 014506 (2014).
- [37] T. Zhou, Y. Gao, and Z. Wang, Phys. Rev. B **93**, 094517 (2016).
- [38] J. Liu, W. Duan, and L. Fu, Phys. Rev. B **88**, 241303 (2013).
- [39] S. Das, L. Aggarwal, S. Roychowdhury, M. Aslam, S. Gayen, K. Biswas, and G. Sheet, Appl. Phys. Lett. **109**, 132601 (2016).